Electrostatically actuated failure of microfabricated polysilicon fracture mechanics specimens†

BY H. KAHN[1], R. BALLARINI[2], R. L. MULLEN[2] AND A. H. HEUER[1]

[1] Department of Materials Science and Engineering,
[2] Department of Civil Engineering, Case Western Reserve University,
10900 Euclid Avenue, Cleveland, OH 44106, USA

Polysilicon fracture mechanics specimens have been fabricated using standard microelectromechanical systems (MEMS) processing techniques, and thus have characteristic dimensions comparable with typical MEMS devices. These specimens are fully integrated with simultaneously fabricated electrostatic actuators, which are capable of providing sufficient force to ensure catastrophic crack propagation from blunt notches produced using micromachining. Thus, the entire fracture experiment takes place on-chip, without any external loading source. Fracture has been initiated using both monotonic and cyclic resonance loading. A reduction in the nominal toughness under cyclic loading is attributed to subcritical growth of sharp cracks from the micromachined notches in the fracture mechanics specimens. Fatigue fracture has been observed in specimens subjected to as many as 10^9 cycles, and environmental corrosion is implicated in at least some aspects of the fatigue.

Keywords: polysilicon; fracture; fatigue; microfracture; electrostatic actuation; microelectromechanical systems (MEMS)

1. Introduction

Polysilicon is the most commonly used structural material for surface micromachined microelectromechanical systems (MEMS) devices. (Surface micromachining refers to the production of complex pseudo-two-dimensional structures containing fine details onto a substrate by an *additive* process (such as chemical vapour deposition (CVD)) involving masks generated using photolithographic technology. This additive process is distinguished from bulk micromachining, which is a *subtractive* process involving controlled etching of fine details into a substrate using a photolithographically generated etch-resistant mask. Many MEMS devices are fabricated using both surface and bulk micromachining. See Madou (1997) for further details on MEMS processing.) However, the ability to predict the long-term reliability of these structures is quite primitive; the fatigue and fracture behaviour of this material are not known on the relevant size scale. (Typical dimensions are of the order of micrometres.) In addition, traditional microfabrication processes induce unique surface modifications,

† The authors dedicate this paper to the memory of Dr Haian Luo.

novel processing-induced defects, and significant residual stresses, all of which can affect the fracture behaviour and will be discussed further in later sections.

Fracture of micromachined polysilicon test specimens has been the subject of several recent reports. Brown *et al.* (1997) determined the moisture-sensitive fatigue life of polycrystalline 'microstructures' subjected to cyclic stresses (the term microstructure is used here in the sense of miniature structures, rather than the sense of grain and defect structure used by materials scientists). Sharpe *et al.* (1998) and Tsuchiya *et al.* (1998) employed external load cells attached to miniature fracture mechanics specimens via adhesives or via electrostatic attraction and determined the critical stress intensity factor K. Their reported values of 1.4 and 1.9 to $4.5 \, \text{MPa m}^{1/2}$, respectively, are associated with a finite radius (0.23–1 μm) notch, and depend on specimen geometry and processing history. The present authors (Ballarini *et al.* 1997) have previously reported J_c (critical energy release rates determined using the J-integral) values of $16–62 \, \text{N m}^{-1}$. These values are higher than those accepted for single-crystal silicon ($K_{Ic} \approx 0.9 \, \text{MPa m}^{1/2}$; $J_c \approx 4.8 \, \text{N m}^{-1}$).

The present work involves a polysilicon fracture mechanics test specimen fully integrated with a simultaneously microfabricated actuator. This allows on-chip testing of the micromachined specimens without the need of an external loading device.

The characteristic dimensions of our specimens are comparable with typical MEMS devices. The critical displacement of the electrostatic actuator at the instant of fracture is recorded, and subsequent finite-element modelling is used to determine the stress concentration at the notch tip. Since the notch tip is quite blunt (the tip radius is 1 μm), the maximum principal stress and the critical value of the nominal J-integral for fracture initiation, J_c, are reported.

The actuation mechanism exploited to create the necessary far field force for fracture was electrostatic attraction in interdigitated comb structures. (This mechanism is quite robust and is the basis of the widely used accelerometers that comprise most current automotive air-bag sensors.) As illustrated in figure 1*a*, when a voltage is applied between two sets of fingers, the capacitance, C, of the structure will increase as the movable fingers traverse a distance x and increase the finger–finger overlap. The force, F, generated by such electrostatic actuation is given by

$$F = \frac{1}{2}\frac{\partial C}{\partial x}V^2 = n\varepsilon\frac{h}{g}V^2, \tag{1.1}$$

where n is the number of fingers, ε is the permittivity of the fluid between the fingers, h is the height of the fingers, g is the gap spacing between the fingers, and V is the applied voltage (Tang *et al.* 1989). Such electrostatic actuation usually involves only modest numbers of interdigitated combs. However, 400 μN of actuation force have been realized in bulk micromachined single-crystal silicon devices that contained 2000 pairs of interdigitated comb fingers (Saif & MacDonald 1996). We have now generated similarly large electrostatic forces in surface-micromachined polysilicon devices.

2. Experiment

(*a*) *Device*

The device used in this investigation is shown schematically in figure 1*b*. The outer frame of the actuator is fully released from the substrate in the final stage of MEMS
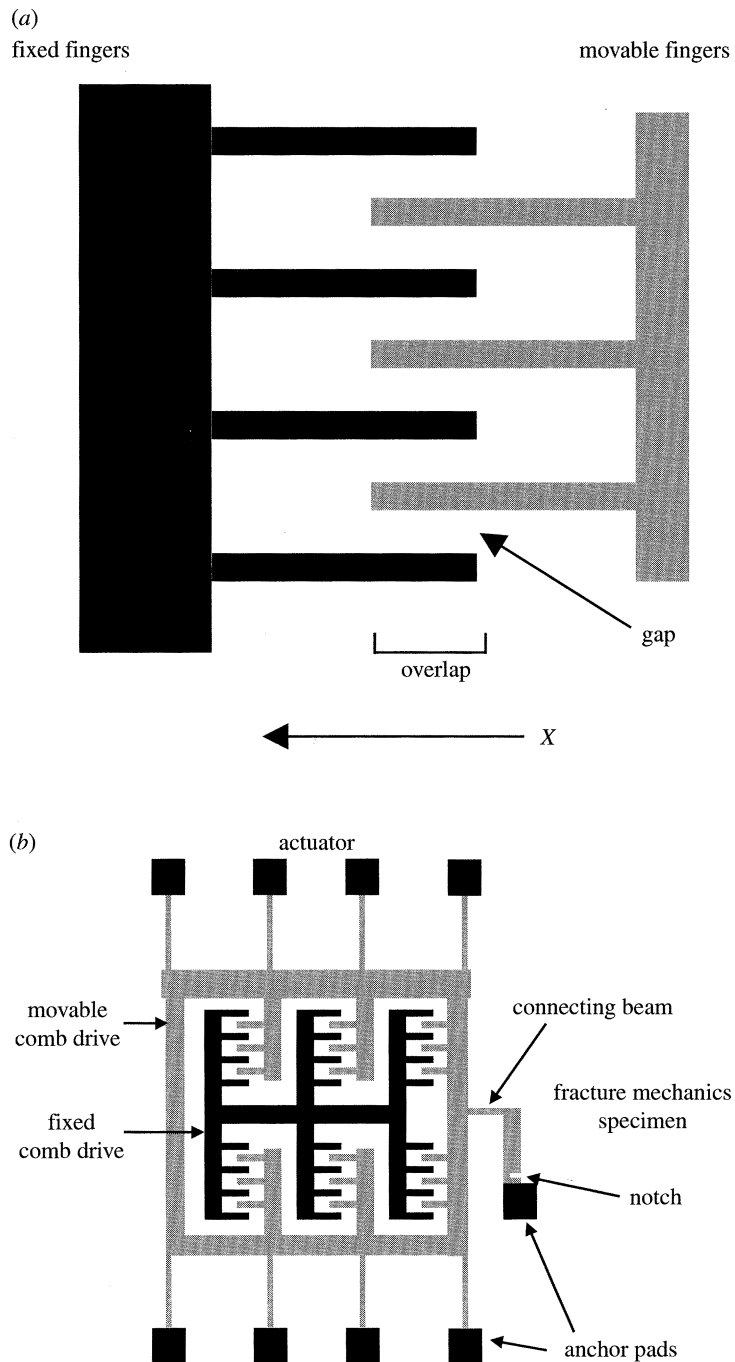
(a)

fixed fingers   movable fingers

gap

overlap

X

(b)   actuator

movable
comb drive   connecting beam

                                                fracture mechanics
fixed   specimen
comb drive

                                                      notch

                                                 anchor pads

Figure 1. (a) Sketch of two sets of interdigitated comb fingers; when a voltage is applied across this comb drive, the movable fingers will move to the left; (b) schematic drawing of the fracture device which consists of an actuator (in this sketch, the actuator has 18 pairs of comb fingers acting in parallel) and a fracture mechanics specimen.
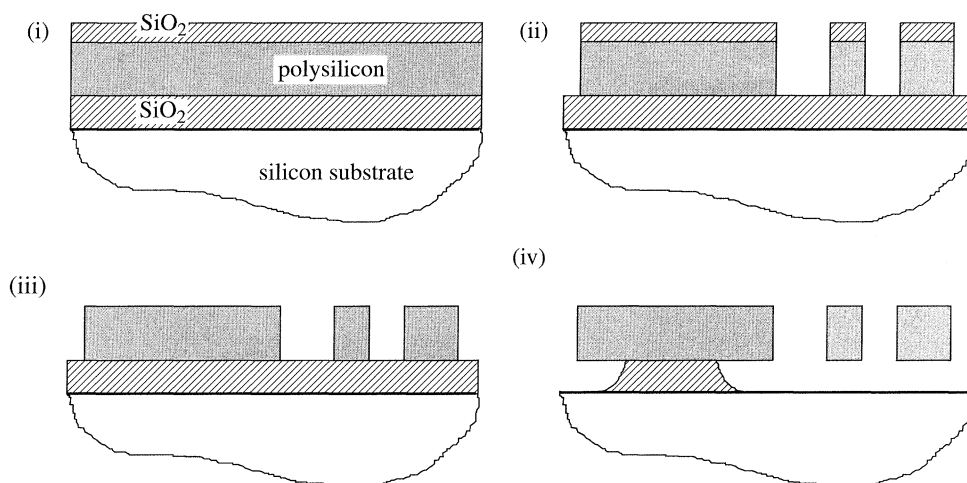
Figure 2. Cross-sectional drawings depicting the device fabrication sequence: (i) a thick SiO$_2$ film is grown on a silicon substrate, followed by LPCVD deposition of a polysilicon film and a SiO$_2$ film; (ii) using photolithography, the device is patterned, and the top SiO$_2$ and polysilicon films are sequentially etched; (iii) the top SiO$_2$ film is completely removed, and the polysilicon film is boron-doped; (iv) the device is time-released in hydrofluoric acid, such that some SiO$_2$ remains beneath the large anchor pads, while the smaller features are fully released and free to move.

processing and is free to move when subjected to the electrostatic attraction of the comb drives. The frame is anchored to the substrate at the ends of eight long, thin beams, which constrain movement in the vertical direction, but allow side-to-side movement. Two different devices were fabricated, containing either 1456 or 2040 pairs of comb fingers (rather than the 18 shown in figure 1b), which pull the actuator to the left (in the orientation of figure 1b) when a voltage is applied. This in turn pulls on the connecting beam and the top of the fracture mechanics microdevice, which is anchored to the substrate on the opposite side. This creates a stress concentration at the notch of the specimen, which mimics a conventional single edge-notch fracture mechanics specimen. When the displacement reaches a critical value, the mechanical stresses become sufficiently high to initiate fracture.

(b) Fabrication

The test specimens were fabricated using standard surface-micromachining techniques and a one-mask process, illustrated in figure 2 and summarized as follows. (100) silicon wafer substrates are oxidized to a thickness of 2.5 µm, the oxide serving as a sacrificial layer. A 5.2 µm thick film of polysilicon is deposited by low pressure chemical vapour deposition (LPCVD) at 580 °C using SiH$_4$ gas. The as-deposited film is at least partly amorphous (Harbeke *et al.* 1984), and is annealed at 1100 °C, during which treatment, crystallization to a fine-grained polycrystalline microstructure occurs; the microstructure is shown in the transmission electron micrograph in figure 3. A 0.5 µm film of SiO$_2$ is then deposited by LPCVD at 450 °C using SiH$_4$ and O$_2$ gases for use as a masking oxide. Standard photolithography is then used to pattern the devices in photoresist. Subsequently, the masking oxide is dry-etched in
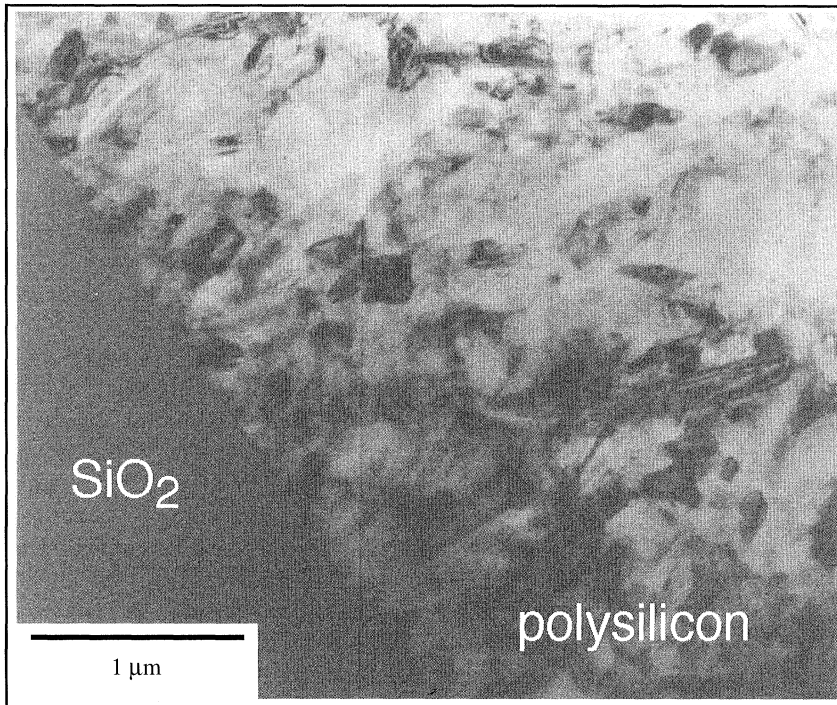
Figure 3. Transmission electron micrograph showing the microstructure of the polysilicon.

a CHF_3/C_2F_6 plasma, followed by dry etching of the polysilicon in a Cl_2 plasma. The remaining masking oxide is chemically removed using HFA, and the polysilicon is boron-doped in a diffusion furnace at 1000 °C. (Such boron-doped polysilicon specimens have a resistivity of 3×10^{-3} Ω cm.) Both the Cl_2 plasma etching and the boron doping create unique surface features on the sidewalls of the polysilicon devices. These will be shown and discussed in the section on fractography.

After doping, the devices are released by immersion in aqueous hydrofluoric acid (HFA) to dissolve some of the SiO_2 for a specific time, such that some oxide remains beneath the anchor pads leaving them attached to the substrate, while the movable portions of the device are fully released. Following HFA release, the devices are placed in a 25% NH_4F solution before rinsing, to help prevent stiction of the moving parts to the substrate.†

A scanning electron micrograph (SEM) of a fabricated 1456 comb device, along with magnified views of the fracture mechanics specimen, are shown in figure 4a–c. (The dimensions of the particular fracture mechanics specimen shown in figure 4c are also listed in table 1 as fracture mechanics specimen A.) The 1456 pairs of comb fingers, situated in 14 rows, are 2 μm wide, 20 μm long, and are too small to be distinguished in the low-magnification SEM image. The 'release holes' visible in the upper portion of the fracture specimen and the outer frame of the actuator allow the HFA etchant to flow beneath these areas during release.

---

† Stiction refers to the immobilization of a micromachined specimen during release. The NH_4F treatment was suggested by Houston *et al.* (1997).

Table 1. *Fracture mechanics specimen dimensions*

(Specimen A is shown in figure 4c. All dimensions are in micrometres.)

fracture mechanics specimen	doped	notch width	tip radius	uncracked ligament length	reduced beam		release end	
					width	length	width	length
A	yes	2	1	4.2	9.4	15	75	156
B	no	2	1	4.5	10	15	75	156
C	no	2	1	3	7	15	40	100

The boron-doped polysilicon contains a residual compressive stress of 32 ± 5 MPa. When the device is released, these residual stresses cause the anchored support beams to buckle slightly, as seen in figure 4d. In addition, the movable portion of the actuators are deflected out-of-plane by these residual stresses, as seen in figure 4e. Both of these geometric changes in the device structure disappear during testing, as described below.

The residual stresses were measured using passive microstrain gauges (Kahn *et al.* 1996), which were simultaneously fabricated on the same wafers. One such device is shown in figure 5a. When released, the ends of the two offset legs remain anchored at the pads (A); any expansion or contraction due to relieved stresses will cause the pointer beam to rotate. Figure 5b shows the end of a pointer beam before release, and figure 5c after release. The measured deflections, along with finite-element modelling of the device, allow us to determine the residual stresses quantitatively.

(c) Experimental procedure

The fracture test is conducted by applying a DC voltage between the fixed and movable sets of comb fingers. This was done on a probe station, with one probe in contact with the central fixed portion of the device, and a second probe in contact with one of the outer anchor pads. A third probe was positioned in contact with the silicon substrate. This last probe was shorted to the probe on the anchor pad, and both were grounded. At the start of each test, the applied voltage had to be increased to a certain level (*ca.* 40 V) before the movable portion of the actuator would be pulled flat (to counteract the processing-induced residual stresses). At this voltage, the movable fingers were nearly in-plane with the fixed fingers (to within *ca.* 1 μm, the resolution of the focusing stage of the optical microscope attached to the probe station). After that point, the support beams were no longer buckled, but rather were deflected in the direction of the actuator motion. As the voltage was further increased, the actuator (and thus the released side of the fracture specimen) moved by increasing amounts until a crack emanated from the micromachined notch and fracture ensued. At this time, the fingers immediately moved into contact with each other, shorting the device and causing some melting of the polysilicon. During the test, the displacement of the actuator was recorded visually, with an accuracy of ± 0.3 μm.

Devices were also fabricated from polysilicon films that were not boron-doped, but were otherwise processed identically. For these devices, the geometry of the fracture specimens (fracture mechanics specimen B in table 1) was essentially identical to the doped devices, except that the reduced beam width was 10 μm and the uncracked
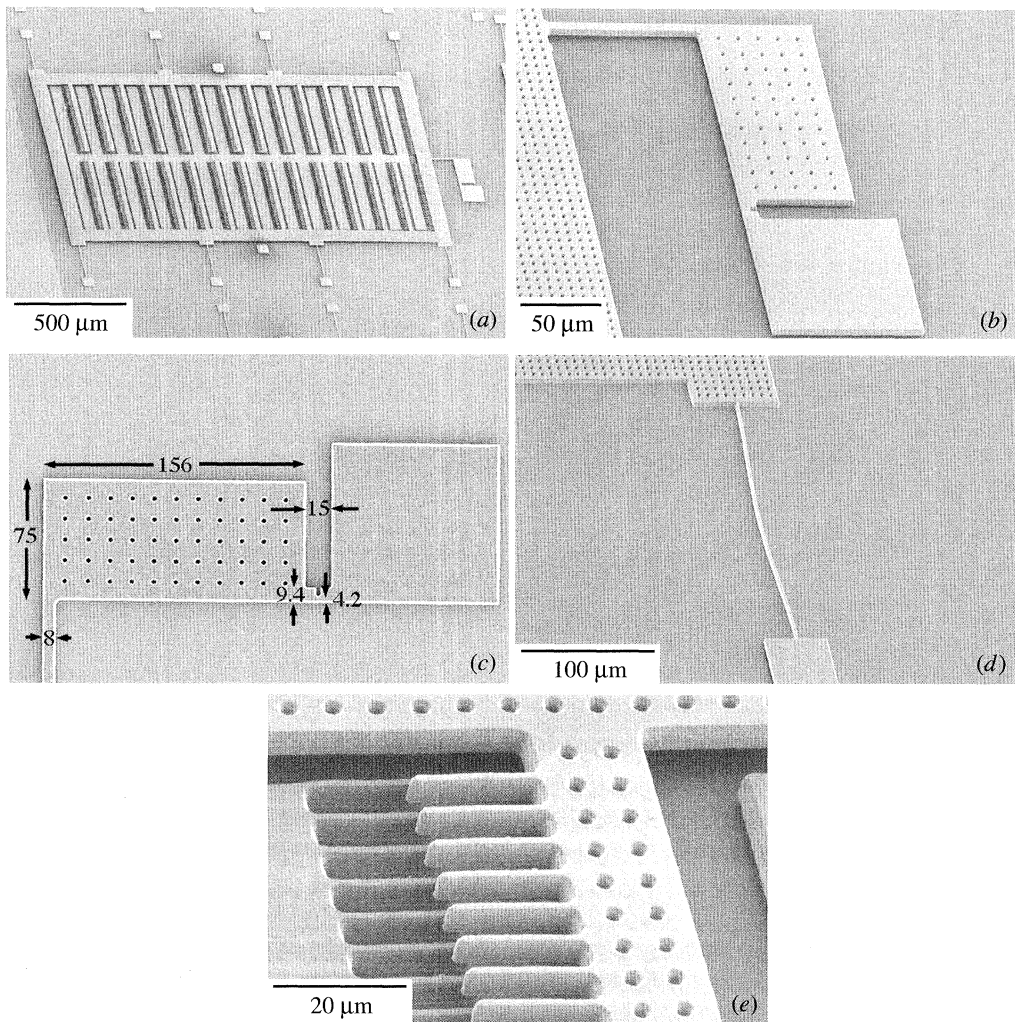
Figure 4. (*a*) SEM image of the entire fracture device (viewed at a 45° angle); (*b*) a close-up of the fracture mechanics specimen. (*c*) A top view of the fracture mechanics specimen (rotated 90°) showing the dimensions (in micrometres); (*d*) one of the device's long support beams, buckled as-fabricated due to compressive residual stresses; (*e*) a high-magnification image showing several of the comb fingers; the fixed and movable combs are not co-planar.

ligament length was 4.5 µm. To achieve sufficient conductivity to allow electrostatic actuation, these devices were sputter-coated with *ca*. 10 nm of palladium following release. The residual stresses in these devices were smaller, 19 ± 5 MPa, and tensile. This increased the stiffness of the actuator support beams to such an extent that sufficient displacement of the actuator to cause fracture could not be attained. (The force limitation in these specimens arose from the actuation voltage causing the outer frame of the actuator to bend, moving the comb fingers sideways, and shorting the device.) However, because of the tensile residual stress, the support beams were not buckled, and the application of an AC signal, at the proper frequency (*ca*. 20 kHz),
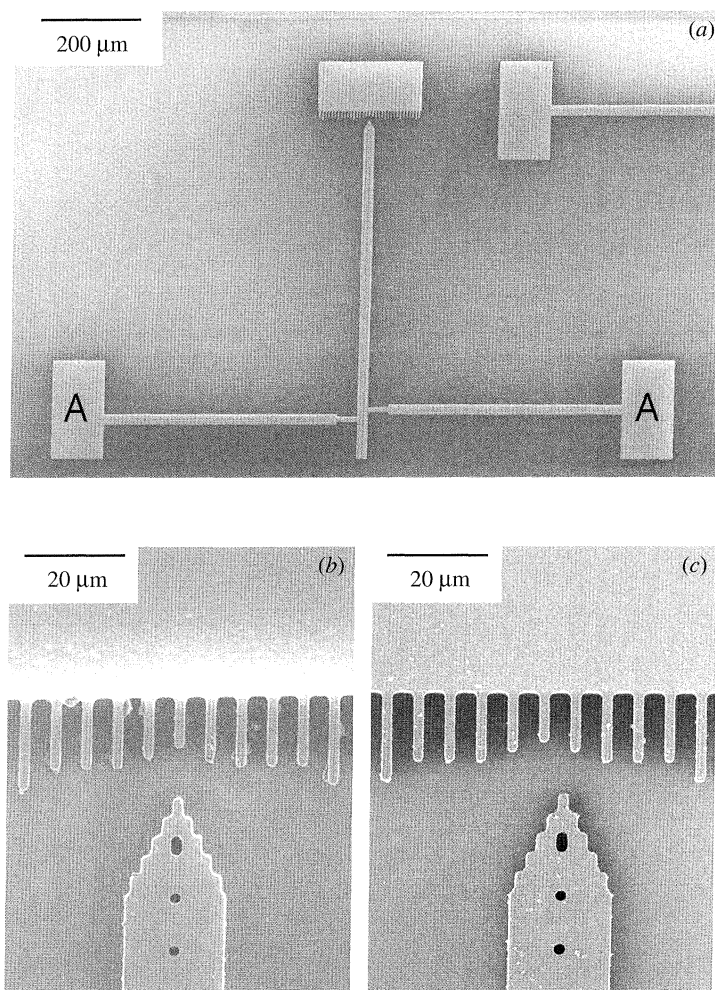
Figure 5. (*a*) SEM image of a micromachined passive strain gauge, with close-ups of the end of the pointer beam (*b*) before release and (*c*) after release.

caused the device to resonate. While in resonance, a sufficiently high amplitude displacement could be achieved with a relatively low voltage to cause catastrophic crack propagation and fracture of the specimen. To investigate the effects of the laboratory ambient on fatigue behaviour, in particular the relative humidity, some resonance tests were performed in a vacuum chamber, which was evacuated to a pressure of 8 Pa.

Though these devices could not be fractured with a DC signal, monotonic fracture could still be accomplished by mechanically pushing the actuator with a probe, as in our previous work (Ballarini *et al.* 1997). The probe was carefully manipulated to ensure strictly lateral stresses; though for this experiment, the possibility of perpendicular and out-of-plane stresses could not be eliminated. For completeness, boron-doped devices were also tested with the mechanical probe technique, and the results included here.

(d) Modelling

After determining the displacement at which fracture occurred, the device behaviour under electrostatic loading was thoroughly modelled using finite-element analysis (FEA) in order to determine the relationship between the observed displacement at fracture and the maximum tensile stresses, σ_{max}, as well as the critical energy release rates, J_c. The finite-element model included both the fracture mechanics specimen and the actuator. The geometry of the fracture specimen was determined from measured values while the dimensions of the actuator were taken from nominal design values. The model was constructed from *ca.* 16 000 eight-node plane stress quadrilateral elements. The mesh density was determined by a study of the convergence of the strain energy with number of elements. For all analyses, Young's modulus and Poisson's ratio of polysilicon were assumed to be 168 GPa and 0.22, respectively, and a large strain formulation was used. Experimentally measured residual stresses were included. Figures 6 and 7 present typical results of the finite-element calculations. Figure 6 shows the magnified displacements of both the actuator and specimen for a 600 µN load on a boron-doped device. The effect of residual stress on the upper right support beam can be seen in the displaced shape. In addition, the moment generated in the fracture specimen results in a small rotation of the actuator. Figure 7a shows the discretization of the specimen geometry and the contours of displacement magnitude. Contours of maximum tensile stress in the region surrounding the notch tip are shown in figure 7b. The residual stress (the stiffness of the support beams) has a significant impact on the actuator behaviour; however, σ_{max} in the fracture specimens was independent of residual stress for actuator displacements resulting in fracture. For example, at a 7 µm displacement of the end of the fracture specimen, σ_{max} was calculated to be 4.07 MPa in a linear analysis without residual stress and 4.09 MPa using large strain and residual stresses. Reported stress and energy release values presented are calculated from nonlinear finite-element results. Linear calibrations can be used with less than a 5% difference from the nonlinear calculation. For the boron-doped devices, the linear calibrations indicated that $J_c = 1.27\delta^2$ and $\sigma_{max} = 0.58\delta$, where δ is the displacement of the end of the fracture mechanics specimen in micrometres, J_c is in N m^{-1}, and σ_{max} is in GPa. For the undoped devices, $J_c = 1.38\delta^2$ and $\sigma_{max} = 0.61\delta$. Since displacement was experimentally measured at a specific point on the actuator, FEA modelling was also used to correlate that measurement to the displacement of the specimen.

The FEA modelling also determined that the electrostatic actuator generated 90% of its theoretical force, as calculated by equation (1.1). Most likely, the modest loss in force is due to the fixed and movable fingers not being exactly co-planar during the experiment and to the slight rotation of the actuator.

3. Experimental results and discussion

(a) Monotonic and cyclic fracture

The deflection of a typical sample during monotonic DC loading is shown in figure 8. The specimen fractured at a displacement of 8.3 µm. The movement of the actuator increased linearly with the square of the applied voltage, as expected from the electrostatic force equation (1.1).
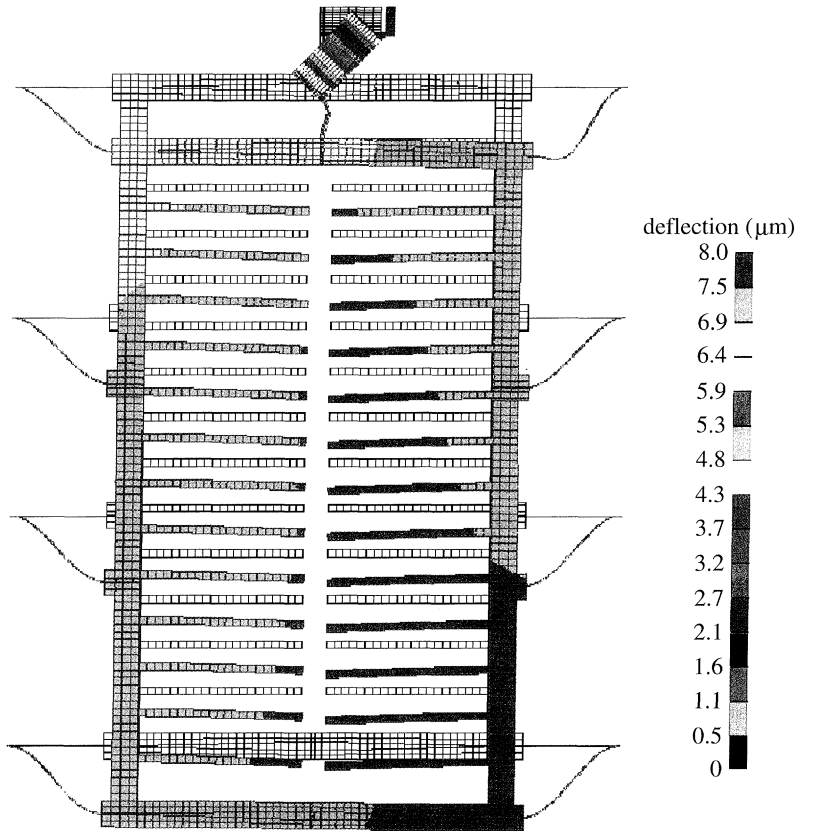
Figure 6. Finite-element calculations showing displacements of a boron-doped device under a 600 μN electrostatic load. The sketch greatly exaggerates the displacements; the original position of the device is outlined in blue.

The displacements at the point of fracture, along with the calculated J_c and σ_{max} values, for the five sets of experiments are shown in table 2. The results for the two different techniques of monotonically loading the boron-doped samples (DC electrostatic actuation and pushing with a probe) are very consistent. This suggests that the two techniques are equivalent.

The J_c values obtained for the monotonically loaded boron-doped and undoped polysilicon devices are comparable with, and consistent with previously reported values for specimens with similar blunt notches (Ballarini *et al.* 1997). The small differences between the boron-doped and undoped samples are within the scatter of the data; therefore, any doping effects on toughness must be small or non-existent. The doping procedure also induces some changes in the surface morphology of the polysilicon devices. Because a small amount of oxidation occurs, followed by the removal of this oxide during the release process, any sharp features will be somewhat rounded. In addition, during the doping, thermal grooving occurs where the grain boundaries intersect the free surface. Both of these features can be seen in the micrographs presented in figure 11.

For the undoped devices, the J_c values derived under cyclic stress are lower than under monotonic loading. This suggests that a sharp fatigue crack initiates during
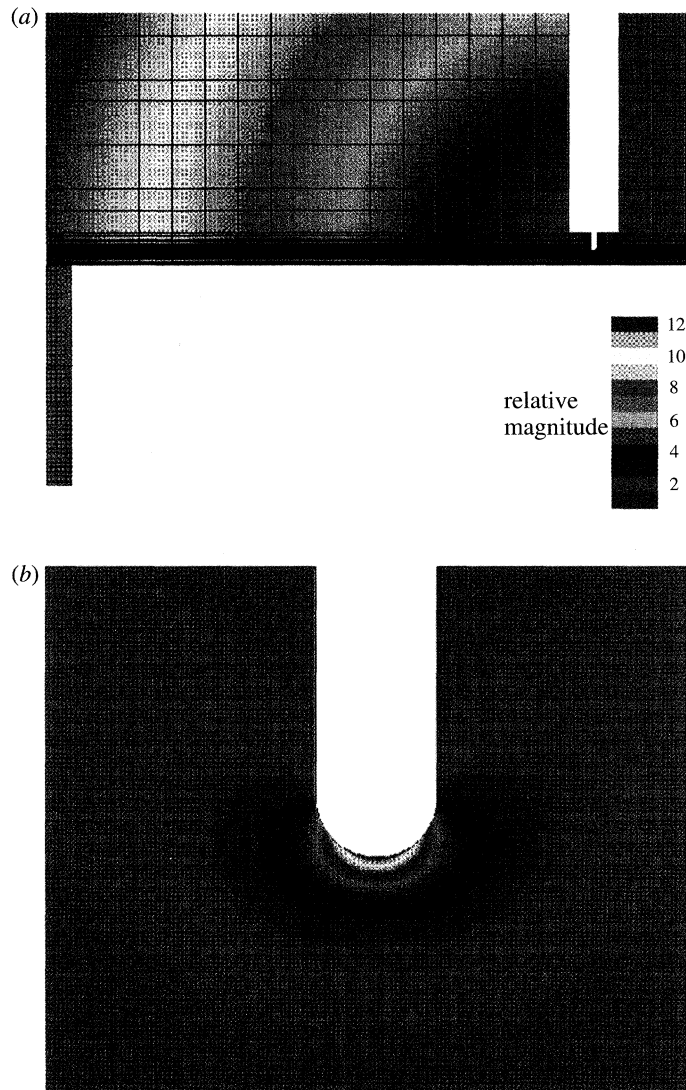
Figure 7. Finite-element calculations showing (*a*) the discretization of the specimen geometry and the contours of displacement magnitude and (*b*) the contours of maximum tensile stress in the region surrounding the notch tip.

the resonance and propagates to a critical dimension. (During the resonance experiments, the specimens were subjected to the critical displacement amplitudes for *ca.* 0.1–5 s before fracture, corresponding to 2000–100 000 cycles. This is referred to as 'fast fracture'.) Additional specimens were set into resonance at displacements that were too low to initiate fast fracture. The specimens were allowed to continue resonating until fracture occurred. The results, including those from the fast fracture and monotonic experiments, are plotted in figure 9 as the maximum tensile stress
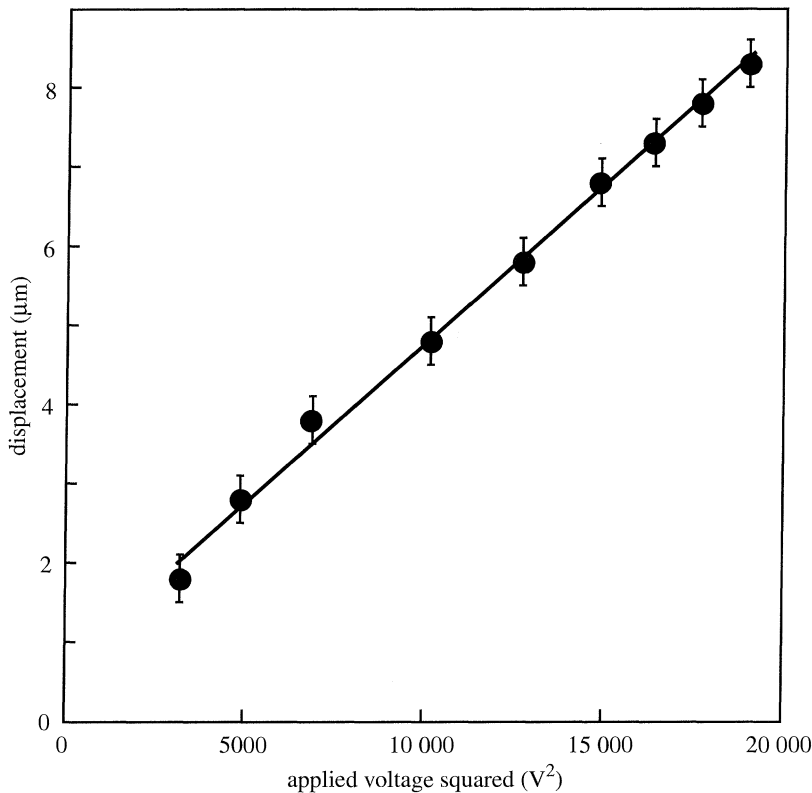
Figure 8. The displacement of the fracture device versus the square of the applied voltage; the device fractured at 8.3 μm displacement.

generated at the notch, σ_{max} versus the number of cycles required for fracture; in essence, this is a traditional S–N (stress to failure versus number of cycles to failure) fatigue curve. All of these tests were carried out in a laboratory ambient, $ca.\,23\,^{\circ}$C and 40% relative humidity. The results represented by circles were obtained using the fracture mechanics specimen described above. The results represented by squares were obtained using a fracture mechanics specimen with the same shape but different dimensions; these specimens are listed as geometry C in table 1. The notch width and tip radius were identical in both specimens. Both specimens were modelled using FEA to determine σ_{max} as a function of displacement, and therefore all the results are included in the same plot.

Figure 9 illustrates that a large scatter exists in the data, possibly due to differences in the roughness of the inside notch surface caused by dry etching, and that fatigue fracture can be achieved at subcritical stresses after as many as 10^9 cycles.

For cyclic loading at low pressures, the J_c values obtained are higher than for cyclic loading in air, but are lower than for monotonic loading. This suggests that fatigue crack initiation and growth occurs during cyclic loading in both environments, but the process is faster in air, presumably due to stress corrosion in the presence of humidity. In the low pressure ambient, stress corrosion at crack tips will be less severe, but mechanical damage can still occur during the tensile–compression fatigue cycles.

Table 2. *Experimental polysilicon fracture data*

	displacement at fracture (µm)	J_c (N m^{-1})	σ_{max} (GPa)
B-doped polysilicon	5.0[a]	31	2.9
	6.3	50	3.6
monotonically loaded	7.1	64	4.1
(DC electrostatically)	7.3[a]	67	4.2
	7.8	77	4.5
(specimen A)	8.3	87	4.8
average	7.0	63	4.0
standard deviation	1.2	20	0.7
B-doped polysilicon	5.5[a]	38	3.2
	6.0[a]	46	3.5
monotonically loaded	6.8[a]	58	3.9
(pushed with probe)	6.8[a]	58	3.9
	6.8[a]	58	3.9
	7.2[a]	67	4.2
(specimen A)	7.3	67	4.2
	7.3	67	4.2
	7.3	67	4.2
	7.4[a]	70	4.3
	7.9[a]	79	4.6
	8.0	81	4.6
	8.5	92	4.9
average	7.1	65	4.1
standard deviation	0.8	14	0.5
undoped polysilicon	7.4[a]	76	4.5
	7.4	76	4.5
monotonically loaded	7.6	80	4.6
(pushed with probe)	7.9	87	4.8
	7.9	87	4.8
	8.2[a]	94	5.0
(specimen B)	9.0	111	5.5
	9.0	111	5.5
average	8.1	90	4.9
standard deviation	0.6	14	0.4

Suresh (1991) reported this phenomenon for zero stress–compression fatigue cycles in ceramic composites, and attributed irreversible deformations to microcracking and friction. We are now searching for the sources of the inelasticity in polysilicon.

(b) Fractography

Figure 10 shows the top view of a fractured specimen. The crack path, is significantly deflected; this was observed in most specimens. The fracture surface from a

Table 2. *Cont.*

	displacement at fracture (µm)	J_c (N m^{-1})	σ_{max} (GPa)
undoped polysilicon	4.6	29	2.8
	4.6	29	2.8
cyclically loaded	4.9	33	3.0
	5.0	35	3.1
(at atmospheric pressure)	5.3	39	3.2
	5.3	39	3.2
(specimen B)	6.0	50	3.7
	6.6	60	4.0
average	5.3	39	3.2
standard deviation	0.7	11	0.4
undoped polysilicon	4.4	26	2.7
	5.3[a]	39	3.2
cyclically loaded	5.3[a]	39	3.2
	6.5[a]	58	4.0
(at low pressure)	7.2	72	4.4
(specimen B)	8.7	105	5.3
average	6.2	63	4.0
standard deviation	1.6	27	0.9

[a]These devices contained actuators with 2040 pairs of comb fingers; all other devices had actuators with 1456 pairs of comb fingers.

boron-doped specimen, which fractured under monotonic loading at a deflection of 7.9 µm, is shown in figure 11*a*, *b*, and from an undoped specimen, which fractured under cyclic loading at a deflection of 5.3 µm, in figure 11*c*, *d*. (These were the two best examples of 'classical' fracture features that were observed.) In both samples, a semicircular 'mirror' is present, characteristic of brittle fracture, and surrounds the crack-initiating flaw. Beyond the relatively smooth mirror zone, branching cracks can be seen radiating from the crack initiation site. In brittle ceramics, the radius of the mirror is known to be 6–10 times the radius of the original flaw (Mecholsky 1994). For a semicircular flaw, the stress intensity factor is given by

$$K = 1.25S\sqrt{a}, \tag{3.1}$$

where S is the nominal stress, and a is the flaw radius (Mecholsky 1994). Using the values of σ_{max} from table 2 for S, this corresponds to a fracture toughness, K_{Ic}, of 2.1–2.7 MPa m$^{1/2}$ for boron-doped polysilicon and 1.1–1.4 MPa m$^{1/2}$ for undoped polysilicon, using a values of 0.13–0.22 µm and 0.07–0.12 µm, respectively. It should be emphasized that this analysis is valid only for perfectly semicircular flaws that lie perpendicular to the stress axis, a fact that could not be determined in this experiment. Therefore, the differences seen between the doped and undoped polysilicon K_{Ic} values may not be significant.

These values are still higher than values previously reported for single-crystal silicon (*ca.* 0.9 MPa m$^{1/2}$). The higher fracture toughness of polysilicon compared with single-crystal silicon results from the finite radius notch and possibly also
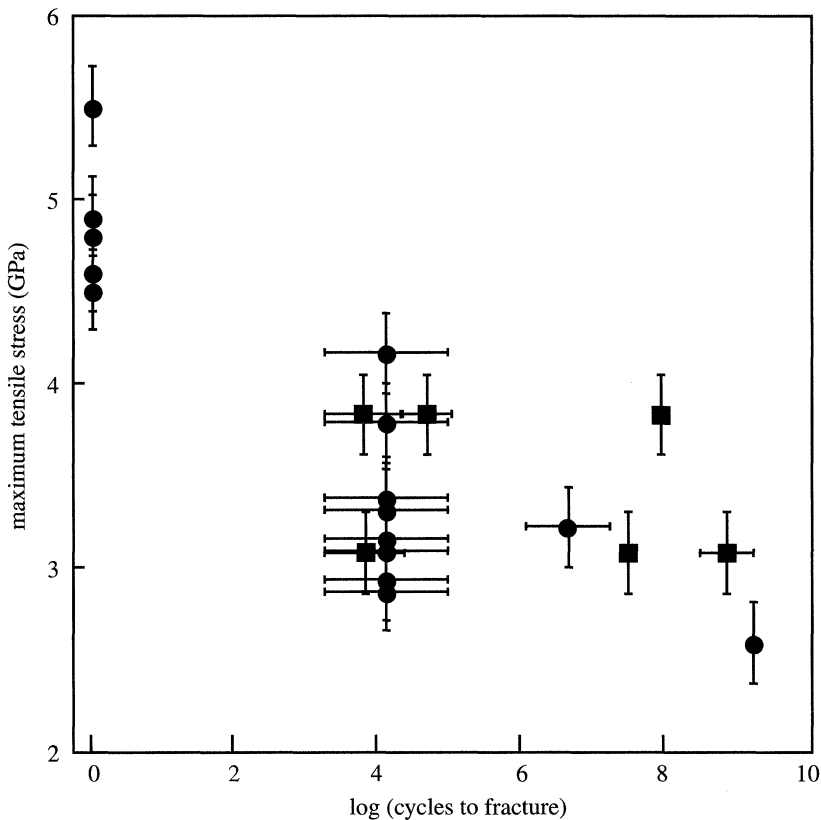
Figure 9. *S–N* (stress to failure versus number of cycles to failure) curve for fatigue fracture. See text for further details.

from 'microstructural' toughening in our fine-grained polycrystalline samples. Current research is now being devoted to producing microfabricated fracture mechanics specimens containing atomically sharp cracks to study this phenomenon and other aspects of the fatigue of polysilicon (effects of humidity, temperature, etc.).

4. Summary and conclusions

The fracture behaviour of surface-micromachined polysilicon has been investigated for the first time using an integrated micromachined loading device, which employs electrostatically actuated comb drives to generate sufficient force to achieve catastrophic crack propagation. Fracture specimens were stressed statically and dynamically to achieve fast fracture. The data suggest that when the device is cyclically loaded, an atomically sharp crack develops at the root of the notch. Dynamic stressing below the critical crack opening displacement for fast fracture also results in fatigue fracture after an increased number of cycles. The fatigue effect appeared to be more serious when testing was carried out in air at atmospheric pressure (10^5 Pa) than at low pressure (8 Pa).
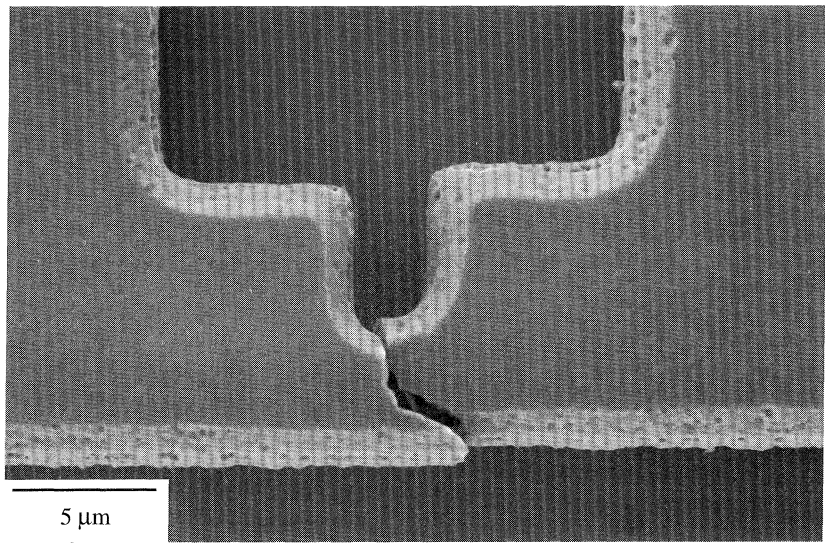
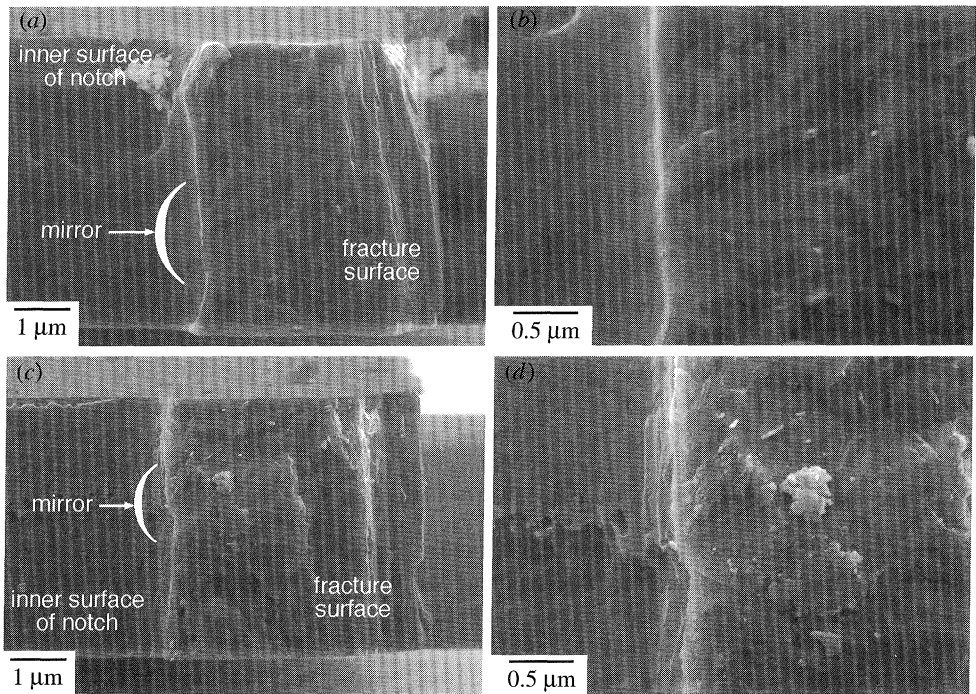Figure 10. SEM image of a fractured specimen, top view.

Figure 11. SEM images of (a) the fracture surface of a boron-doped specimen; (b) higher magnification image of the area surrounding the crack initiation site; (c) the fracture surface of an undoped specimen; (d) higher magnification image of the area surrounding the crack initiation site.

Appendix A.

After this manuscript was submitted, polysilicon fracture mechanics specimens were fabricated with sharp cracks created by Vickers indentation. One specimen was monotonically fractured using DC electrostatic actuation and exhibited a fracture toughness, K_{Ic}, of $1.0 \pm 0.2\,\mathrm{MPa\,m}^{1/2}$.

References

Ballarini, R., Mullen, R. L., Yin, Y., Kahn, H., Stemmer, S. & Heuer, A. H. 1997 The fracture toughness of polysilicon microdevices: a first report. *J. Mater. Res.* **12**, 915–922.

Brown, S. B., Van Arsdell, W. & Muhlstein, C. L. 1997 Materials reliability in MEMS devices. In *Proc. IEEE Int. Conf. on Solid-State Sensors and Actuators, Transducers 97, 16–19 June 1997, Chicago, IL*, pp. 591–593. New York: IEEE.

Harbeke, G., Krausbauer, L., Steigmeier, E. F., Widmer, A. E., Kappert, H. F. & Neugebauer, G. 1984 Growth and physical properties of LPCVD polycrystalline silicon films. *J. Electrochem. Soc.* **131**, 675–682.

Houston, M. R., Howe, R. T. & Maboudian, R. 1997 Effect of hydrogen termination on the work of adhesion between rough polycrystalline silicon surfaces. *J. Appl. Phys.* **81**, 3474–3483.

Kahn, H., Stemmer, S., Nandakumar, K., Heuer, A. H., Mullen, R. L., Ballarini, R. & Huff, M. A. 1996 Mechanical properties of thick, surface micromachined polysilicon films. In *Proc. IEEE Int. Workshop on Micro Electro Mechanical Systems, MEMS 96, 11–15 February 1996, San Diego, CA*, pp. 343–348. New York: IEEE.

Madou, M. 1997 *Fundamentals of microfabrication.* New York: CRC Press.

Mecholsky, J. J. 1994 Quantitative fractographic analysis of fracture origins in glass. In *Fractography of glass* (ed. R. C. Bradt & R. E. Tressler), pp. 37–73. New York: Plenum Press.

Saif, M. T. A. & MacDonald, N. C. 1996 A millinewton microloading device. *Sensors Actuators* A **52**, 65–75.

Sharpe, W. N., Yuan, B. & Edwards, R. L. 1998 Fracture tests of polysilicon film. In *Thin Films—Stresses and Mechanical Properties VII, MRS Symp. Proc., 1–5 December 1997, Boston, MA* (ed. R. C. Cammarata, M. Natasi, E. P. Busso & W. C. Oliver), vol. 505, pp. 51–56. Pittsburgh, PA: Materials Research Society.

Suresh, S. 1991 *Fatigue of materials.* New York: Cambridge University Press.

Tang, W. C., Nguyen, T.-C. H. & Howe, R. T. 1989 Laterally driven polysilicon resonant microstructures. *Sensors Actuators* **20**, 25–32.

Tsuchiya, T., Sakata, J. & Taga, Y. 1998 Tensile strength and fracture toughness of surface micromachined polycrystalline silicon thin films prepared under various conditions. In *Thin Films—Stresses and Mechanical Properties VII, MRS Symp. Proc., 1–5 December 1997, Boston, MA* (ed. R. C. Cammarata, M. Natasi, E. P. Busso & W. C. Oliver), vol. 505, pp. 285–290. Pittsburgh, PA: Materials Research Society.